




Ab initio investigation of the structural, optoelectronic, mechanical, vibrational, and thermoelectric properties of the $\text{Si}_x\text{Sn}_{1-x}\text{Se}$ alloys

Muhammad Atif Sattar^{1,2} , Najwa Al Bouzieh¹, Fayyaz Hussain³, Maamar Benkraouda¹, Nacir Tit^{1,2}, and Nouredine Amrane^{1,*}

¹ Physics Department, College of Science, United Arab Emirates University (UAEU), 15551, Al Ain, UAE

² National Water and Energy Center (NWECC), United Arab Emirates University (UAEU), 15551, Al Ain, UAE

³ Materials Simulation Research Laboratory (MSRL), Department of Physics, Bahauddin Zakariya University, Multan 60800, Pakistan

Received: 2 July 2022

Accepted: 5 November 2022

Published online:

4 January 2023

© The Author(s), under exclusive licence to Springer Science+Business Media, LLC, part of Springer Nature 2023

ABSTRACT

Single-crystal SnSe holds the world record for high thermoelectric performance. However, the efficiency of polycrystalline SnSe is limited due to high thermal conductivity (κ) and low electronic conductivity (σ) compared to single-crystal SnSe. Here, we report the low κ and high σ on SnSe with Si doping using semi-classical Boltzmann transport theory and first-principles calculations. Our calculated phonon dispersion curves and elastic constants of the $\text{Si}_x\text{Sn}_{1-x}\text{Se}$ alloys (x varied from 0 to 0.25) show the thermodynamic and mechanical stability. Our density functional theory (DFT)-calculated elastic moduli of the α -SnSe match well with theoretical and experiment reports. The electronic properties are calculated using diversity of exchange-correlation functionals. The band gap for pristine α -SnSe is estimated to be 0.88 eV using the hybrid functional (HSE06), which is in excellent agreement with the experimental value 0.86 eV. The G_0 - W_0 +Bethe–Salpeter Equation, which incorporates combined electron–electron (e–e) and electron–hole (e–h) interactions, is used to calculate the optical characteristics of pure and Si-alloyed α -SnSe. Our DFT-calculated Seebeck coefficient for $\text{Si}_x\text{Sn}_{1-x}\text{Se}$ alloys for all Si doping concentrations revealed p -type behavior. At 770 K, for $x = 0.25$, $\text{Si}_x\text{Sn}_{1-x}\text{Se}$ is found to have the lowest thermal conductivity of $\sim 0.16 \text{ Wm}^{-1} \text{ K}^{-1}$ attributed to the high lattice anharmonicity. Our results propose a novel strategy to enhance the optical and thermoelectric properties in the SnSe-based thermoelectric materials.

Handling Editor: Ghanshyam Pilania.

Address correspondence to E-mail: namrane@uaeu.ac.ae

<https://doi.org/10.1007/s10853-022-07935-w>

Introduction

Thermoelectric materials have a significant potential for direct transforming waste heat into electricity and providing a long-term solution to the energy problems and growing environmental concerns [1, 2]. The conversion efficiency of thermoelectric material is generally defined as a dimensionless figure of merit ZT , which can be interpreted as $ZT = S^2\sigma T/\kappa$, where σ is the electronic conductivity, S denotes the Seebeck coefficient, T represents the absolute temperature, and κ signifies the sum of electronic (κ_e) and lattice (κ_l) thermal conductivities [3]. An excellent thermoelectric material for practical systems must have the following factors: (i) a high value of Seebeck coefficient to improve the power factor (PF), (ii) maximum voltage and low electrical resistance to limit Joule heat loss, and (iii) lower thermal conductivity to maintain the heat gradient [4]. The complicated interdependence of thermoelectric parameters S , κ_e , and κ_l through carrier concentration (n) concurrently increases the $PF = S^2\sigma$ while lowering the total thermal conductivity ($\kappa = \kappa_e + \kappa_l$). To optimize the ZT of any thermoelectric materials without paying any compromises is indeed a challenging task. These three parameters mainly control the transport properties in any crystal lattice [5]. The lattice thermal conductivity (κ_l) is the least reliant of them [6, 7]. Several practical approaches to optimize thermoelectric performance mainly focused on two prospects. One way to boost the power factor is to use the appropriate dopants suitable for enhancing the carrier concentration [8, 9] and for bandgap engineering [10–12] and producing band resonance levels [13, 14]. Another relatively simple approach is to reduce the lattice thermal conductivity (κ_l) by increasing the phonon scattering rate through dislocations [15–17], all-scale hierarchical architecturing [18], nanostructuring [19, 20], and defect engineering [21, 22].

Single-crystal tin selenide (SnSe) with a layered crystal structure demonstrates world-record thermoelectric performance ($ZT \sim 2.6$ at 923 K along the b -axis), which is made up of toxic-free and earth-abundant elements [8, 23, 24]. Yet, polycrystalline SnSe demonstrates significant competitiveness in the thermoelectric family through recent improvements in the material and sparked much interest. One of the crucial factors contributing to the exceptional electrical transport properties of SnSe is the presence of

several close-to-degenerate electronic valence bands with comparatively anisotropic effective mass [25, 26]. It is suggested that a particular “pudding-mold-like” band can boost the power factor [27]. A large value of ZT is linked to the ultra-low κ_l , which arises due to strong discrepancy in electronegativity between Sn and Se atoms in the multilayer crystal structure [28, 29]. SnSe structure is the outcome of three-dimensional (3D) NaCl structural distortion linked with SnSe₇ polyhedral with four long and three short Sn–Se bonds. The 5s² lone pair of Sn²⁺ is sterically accommodated by these four long Sn–Se bonds, resulting in anharmonicity and anisotropy in the crystal lattice [10]. SnSe has a bandgap of (~ 0.86 eV) and crystallizes into an anisotropic layered orthorhombic structure ($Pnma-62$) at lower temperatures [29]. However, above ~ 750 K, it undergoes a continuous shear phase transition and acquires higher symmetry ($Cmcm-63$) [30, 31]. The bandgap of SnSe also reduces from indirect 0.61 eV ($Pnma-62$) to direct 0.39 eV ($Cmcm-63$) when the displacive phase transition occurs, thus increasing the carrier mobility and electrical conductivity (σ) due to bipolar conduction in the $Cmcm$ phase [29]. Being attributed to the prevalence of native Sn vacant positions [32] and having a small hole carrier concentration ($\sim 10^{17}$), pristine SnSe is a well-known intrinsic p -type semiconductor [33, 34]. Acceptor doping [35, 36], analogue substitutions [37], and experimentally created extrinsic [38] and intrinsic [39, 40] vacancies have all been used to overcome the low intrinsic carrier concentration of SnSe. Up to date, Na-doping has been used as an efficient acceptor to increase carrier concentration in SnSe crystals ($\sim 3 - 5 \times 10^{17}$ at 300K), which results in the excitation of numerous valence bands that are engaged in electronic charge transport and consequently improves the PF and ZT [26, 35–38]. Improving the electrical transport characteristics of p -type SnSe material is an efficient strategy because of its low thermal conductivity.

Alloying or substitutional doping might be a viable technique to tune the carrier concentration in thermoelectric materials, not only to improve the power factor but also to produce point-defect phonon scattering, which in turn lowers the lattice thermal conductivity [36]. GeSe has the same layered orthorhombic crystal lattice as SnSe at room temperature and is a potential thermoelectric material

[36]. At 873 K, 2D SnSe doped with Ge has a high ZT of ~ 2.1 and deterministic *p*-type carrier concentration, resulting in large electrical conductivity and a power factor of $\sim 5.1 \mu\text{W}/\text{cmK}^2$ and lower thermal conductivity [10]. Si, like Ge, at room temperatures, may adopt the same layered orthorhombic structure with SnSe, lowering thermal conductivity. Furthermore, because of the minor electronegativity difference between Si ($X^{\text{Si}} = 1.90$) and Sn ($X^{\text{Sn}} = 1.96$) [41], Si doping might aid in reducing lattice thermal conductivity, enhancing the power factor as well as regulating the hole carrier concentration [42]. Compared to Na, K, and Ag [35, 43, 44], Si and Ge are a simple to process dopant that has been successfully used to improve the transport characteristics of *p*-type SnSe by optimizing carrier concentration [10, 42]. This encourages us to improve the thermoelectric performance of SnSe by Si doping to maximize its thermoelectric properties while reducing lattice thermal conductivity.

In this study, we systematically investigated the effect of Si doping on the structural, optoelectronic, mechanical, vibrational, and thermoelectric properties of α -SnSe by the simultaneous applications of semi-classical Boltzmann transport theory and the density functional theory (DFT). The $\text{Si}_x\text{Sn}_{1-x}\text{Se}$ alloys (with $x = 6.25\%$, 12.5% , 18.75% , and 25%) have been tested and shown to be able to enhance the optical and thermoelectric properties by Si alloying. Moreover, the Voigt–Reuss–Hill method was used to measure the elastic moduli of α -SnSe, which agree well with the theoretical and experimental data. Furthermore, all $\text{Si}_x\text{Sn}_{1-x}\text{Se}$ alloys are vibrationally stable due to the absence of a negative frequency. We obtain the improved electrical conductivity and power factor values along with reduced thermal conductivity by Si-alloying in the α -SnSe. The lattice thermal conductivity decreases versus increasing the Si content; and extremely low lattice thermal conductivity $\sim 0.16 \text{ Wm}^{-1}\text{K}^{-1}$ at 770 K was achieved for the $\text{Si}_{0.25}\text{Sn}_{0.75}\text{Se}$ alloy composition.

Computational methods

We used first-principles calculations based on density functional theory (DFT) to investigate the structural, mechanical, and optoelectronic properties of pristine and Si-alloyed α -SnSe. The DFT calculations

were carried out using the projector augmented plane wave (PAPW) [45] with pseudopotentials as incorporated in the Vienna Ab Initio Simulation Package (VASP) [46, 47]. The exchange and correlation interactions were addressed using the generalized gradient approximation (GGA) with the Perdew–Burke–Ernzerhof (PBE) functional [48]. To predict the electronic bandgap of the Si-alloyed SnSe alloys more accurately, we have also used strongly constrained and appropriately normed (SCAN) semilocal density functional, the modified Becke–Johnson (mBJ) [49], as well as hybrid functional (HSE06) [50] to overcome the difficulty of standard DFT's in underestimating the bandgap. For structural optimization, the convergence criteria to obtain total energy and atomic forces were adjusted to tolerances 10^{-8} eV and $0.02 \text{ eV}/\text{\AA}$, respectively. The plane wave cutoff energy was selected to be 500 eV. We used a $4 \times 12 \times 12$ Γ -centered Monkhorst–Pack mesh in Brillouin zone to calculate the primitive unit cell and a $4 \times 6 \times 6$ Γ -centered Monkhorst–Pack mesh for the phonon calculations to simulate the $1 \times 2 \times 2$ supercell of the Si-alloyed systems. Denser *K*-mesh grids of $8 \times 24 \times 24$ and $9 \times 12 \times 12$ were used for the pristine and Si-alloyed systems to calculate the electronic density of states (DOS), respectively. For the thermoelectric properties, we employed the denser *k*-mesh grids in BoltzTrap2 computations and then used an interpolation factor of 20 which gives sufficiently fine Fourier interpolations and converged values of the transport properties.

“The Phonopy and Phono3py codes were employed to calculate the vibrational and lattice thermal conductivities for the studied systems. Phonopy and Phono3py use the supercell approach, where small displacements were created in the lattice (0.02 \AA in Phonopy and 0.03 \AA in Phono3py). Harmonic and anharmonic interatomic force constants (IFCs) were calculated via VASP by using PBE-GGA functional in response to these displacements. We used the supercell of dimensions $2 \times 2 \times 2$ (for pristine) and $1 \times 2 \times 2$ (for alloyed systems) to calculate the 2nd order force constants. However, to calculate the 3rd order force constant, we used the same supercell of $1 \times 2 \times 2$ for the both pristine and Si-alloyed SnSe systems. For pristine SnSe, the phono3py code generates the 1290 number of supercells with displacements and 19,584 supercells for each of the Si-alloyed SnSe system. The thermal

conductivities were then computed from modal properties evaluated on $28 \times 32 \times 32$ sampling q -point meshes." The thermoelectric performance is evaluated by solving the Boltzmann Transport equation (BTE) within the constant relaxation time and rigid band approximations implemented in BoltzTrap2 [51]. For the non-consistent G_0W_0 computations [52], we used an energy cutoff of 320 eV, including 216 bands and 72 imaginary frequency points, to calculate the optical properties. Based on single-shot G_0W_0 computation, the optical spectra were calculated by solving Bethe–Salpeter Equations (BSE) [25, 53] level of approximation, presenting a standard many-body method for finding the bandgap and optical properties of semiconductors with high accuracy.

Results and discussion

Structural properties

Figure 1 presents the pristine and Si-alloyed optimized crystal structures of the $\text{Si}_x\text{Sn}_{1-x}\text{Se}$ alloys. A series of five kinds of $\text{Si}_x\text{Sn}_{1-x}\text{Se}$ alloys, including pristine, were investigated in this study where $x = 0, 6.25\%, 12.5\%, 18.75\%,$ and 25% . Pure α -SnSe has an anisotropic layered orthorhombic crystal structure consisting of 8 atoms per primitive cell and belongs to the $Pnma$ (No. 62) space group at low temperatures. Sn and Se atoms are covalently bounded within the layers and form zigzag chains along the b axis, but those between them are weakly attached via a weak van der Waals-forces [54]. The α -SnSe experiences a continuous structural phase transition from the $Pnma$ to the $Cmcm$ phase at a high temperature of about 750 K. In this article, we focused on the $Pnma$ phase of α -SnSe. The primitive unit cell of the pristine α -SnSe ($Pnma$) and Si-alloyed SnSe alloys has been fully relaxed. Our DFT-obtained lattice constant for the pristine α -SnSe ($a = 11.79, b = 4.21,$ and $c = 4.52 \text{ \AA}$) agree with our previous theoretical studies and other DFT results [55, 56]. The experimental lattice constants for the α -SnSe ($a = 11.50, b = 4.15,$ and $c = 4.44 \text{ \AA}$) are slightly lower than our DFT-calculated values because GGA functional overestimates the experimental lattice parameters [57]. The change in space group and lattice parameters should be attributed to the inclusion of Si atoms into the SnSe lattice. The structure optimization for $\text{Si}_x\text{Sn}_{1-x}\text{Se}$

reveals the lattice symmetry reduction upon incorporating a slightly smaller sized Si atom than the Sn atom. It is found that Si doping changes the space group of α -SnSe from orthorhombic ($Pnma$, No. 62) to monoclinic (Pm , No. 6) for $\text{Si}_x\text{Sn}_{1-x}\text{Se}$ alloys. The lattice constants for monoclinic $\text{Si}_{0.0625}\text{Sn}_{0.9375}\text{Se}$ alloys in $1 \times 2 \times 2$ supercells are $a = 11.321, b = 8.211,$ and $c = 8.726 \text{ \AA}$. Further introduction of Si content (at $x = 12.5\%, 18.75\%,$ and 25%) does not change the lattice parameter significantly, implying that Si atoms are incorporated into the host matrix of $\text{Si}_x\text{Sn}_{1-x}\text{Se}$ without further changing the crystal structure, which can be seen from Fig. 1. All the studied alloyed structures, comprising 1–4 Si atoms per computational supercell, are shown to be thermodynamically stable through total energy and phonon-spectra calculations, as described in the sub-sections below. Furthermore, it is crucially important to assess the effect of disorder (i.e., alloying heterogeneity) on the electronic structure and the discussion of this is elaborated in the Appendix.

Electronic properties

The two atom-thick SnSe blocks are heavily corrugated, resulting in a zigzag folded accordion-like projection along the b -axis that determines their remarkable electronic properties. Figure 2 presents simultaneously the electronic band structure along the high symmetry lines in the Brillouin zone (BZ) and the density of states (DOS) plot for the pristine α -SnSe and Si-alloyed $\text{Si}_x\text{Sn}_{1-x}\text{Se}$ at $x = 0.25$ calculated with the meta GGA-mBJ functional. The valence band maxima (VBM) and conduction band minima (CBM) are located along the Γ -Z and Γ -Y high-symmetry lines of the BZ, respectively. With the PBE-GGA potential, we observed an indirect bandgap of 0.56 eV for α -SnSe, which is low relative to the experimental value but compatible with our earlier DFT-reported computations 0.56 eV [55], 0.60 eV [56], 0.65 eV [58], and 0.63 eV [59]. PBE-GGA underestimates the bandgap for semiconductors [60], which significantly impacts the thermoelectric and optical characteristics. To resolve this issue, we estimated the electronic bandgap by involving computationally inexpensive meta-GGA-SCAN and -mBJ functionals, as well as computationally expensive hybrid HSE06 functional. This latter method is well-known for producing reliable and accurate electronic bandgaps. The results of bandgap for α -SnSe using

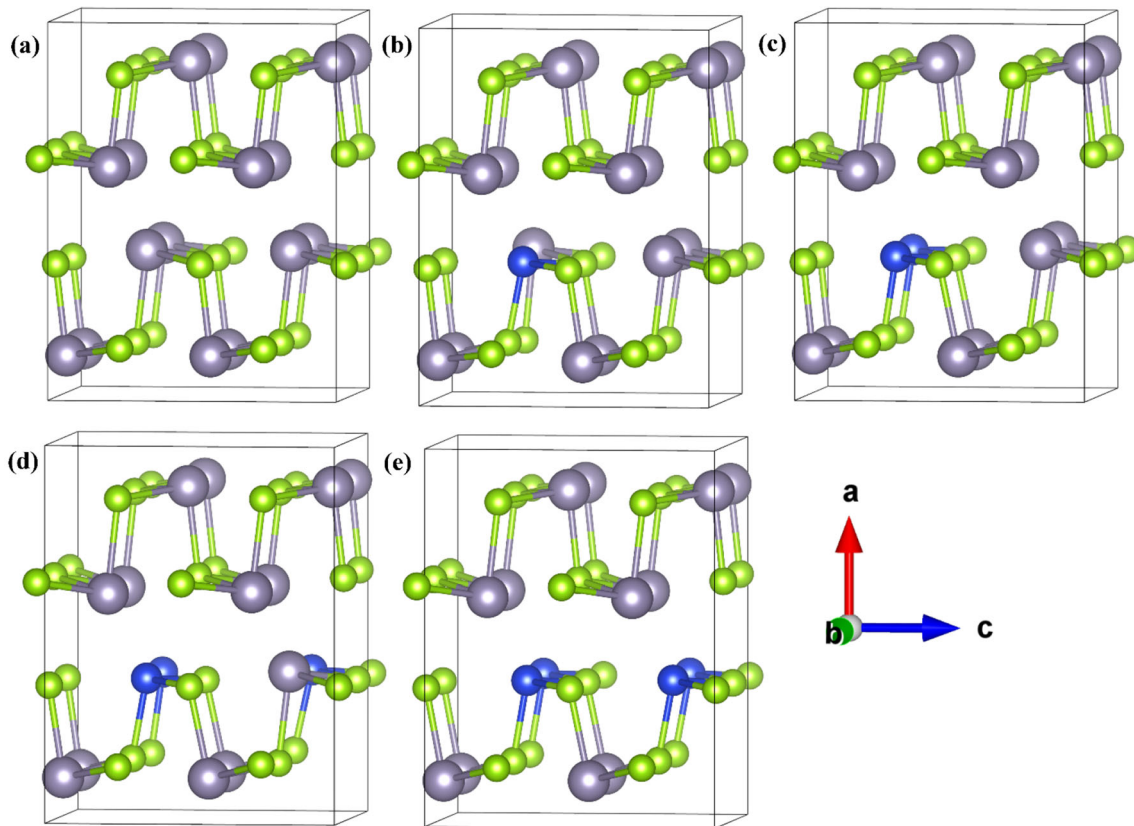


Figure 1 Optimized structures of the $1 \times 2 \times 2$ supercell of **a** pure SnSe and Si-alloyed **b** $\text{Si}_{0.0625}\text{Sn}_{0.9375}\text{Se}$ **c** $\text{Si}_{0.125}\text{Sn}_{0.875}\text{Se}$ **d** $\text{Si}_{0.1875}\text{Sn}_{0.8125}\text{Se}$ **e** $\text{Si}_{0.25}\text{Sn}_{0.75}\text{Se}$. Alloys, where gray, green, and

blue color denotes the Sn, Se, and Si atoms, respectively. **f** Suggested k -path for the monoclinic Si doped SnSe alloys.

the SCAN, MBJ, and HSE06 functionals is 0.75 eV, 0.96 eV, and 0.88 eV, respectively. Table 1 shows the electronic bandgap values for our DFT-investigated pristine and Si-alloyed α -SnSe materials via alloying different functionals. For the pristine α -SnSe, the experimental values are also provided in Table 1 for comparison. The experimental 0.86 eV [29] and other theoretical (0.93 eV) derived values [61] of α -SnSe agree reasonably well with our DFT-predicted values via involving meta-GGA mBJ and HSE06 functionals, 0.98 and 0.88 eV, respectively. We found that the HSE06 functional gives the consistent bandgap values close to the experimental values superior to the other PBE, SCAN, and mBJ exchange–correlation functionals. So, for the α -SnSe, we have demonstrated the DOS and band structure using the meta-GGA mBJ functional, while the electronic properties of the Si-alloyed $\text{Si}_x\text{Sn}_{1-x}\text{Se}$ materials are presented using HSE06 functional.

The α -SnSe is an indirect semiconductor with a “pudding-mold-like” form, as shown in Fig. 2, in

agreement with the results of previous studies [29, 62]. From Fig. 2, it can be seen from both band structure and DOS plot of the α -SnSe that Se p -states dominate the structure of the valence band, whereas the p -states of Sn contribute to the conduction band region. The Sn s -states, which are pretty distant from the Fermi energy, are found below Fermi level by about -4.5 eV. The band structure reveals the covalent bonding with strong ionic character taking place in α -SnSe. Meanwhile, it also shows the considerable discrepancy in electronegativity between Sn and Se atoms (i.e., $X^{\text{Sn}} = 1.96$ Pauling $<$ $X^{\text{Se}} = 2.55$ Pauling), which makes the electrons tend to reside near Se more than Sn atoms [41]. The electronic band structure and DOS plots for the monoclinic $\text{Si}_x\text{Sn}_{1-x}\text{Se}$ alloys (where $x = 6.25\%$, 12.5% , 18.75% , and 25%) calculated with the hybrid HSE06 functional are presented in Figs. 3 and 4, respectively. All $\text{Si}_x\text{Sn}_{1-x}\text{Se}$ alloys are indirect bandgap semiconductors, with their bandgap values found to be in the range of 0.85 eV to 0.92 eV. It is observed that by increasing

Figure 2 Electronic band structure (on the left panel) and the DOS plot (on the right panel) of the **a** pristine α -SnSe and **b** $\text{Si}_{0.25}\text{Sn}_{0.75}\text{Se}$ materials calculated with the meta GGA-mBJ functional [49]. Green, blue, and red colors show contribution of Sn-s, Sn-p, and Se-p states.

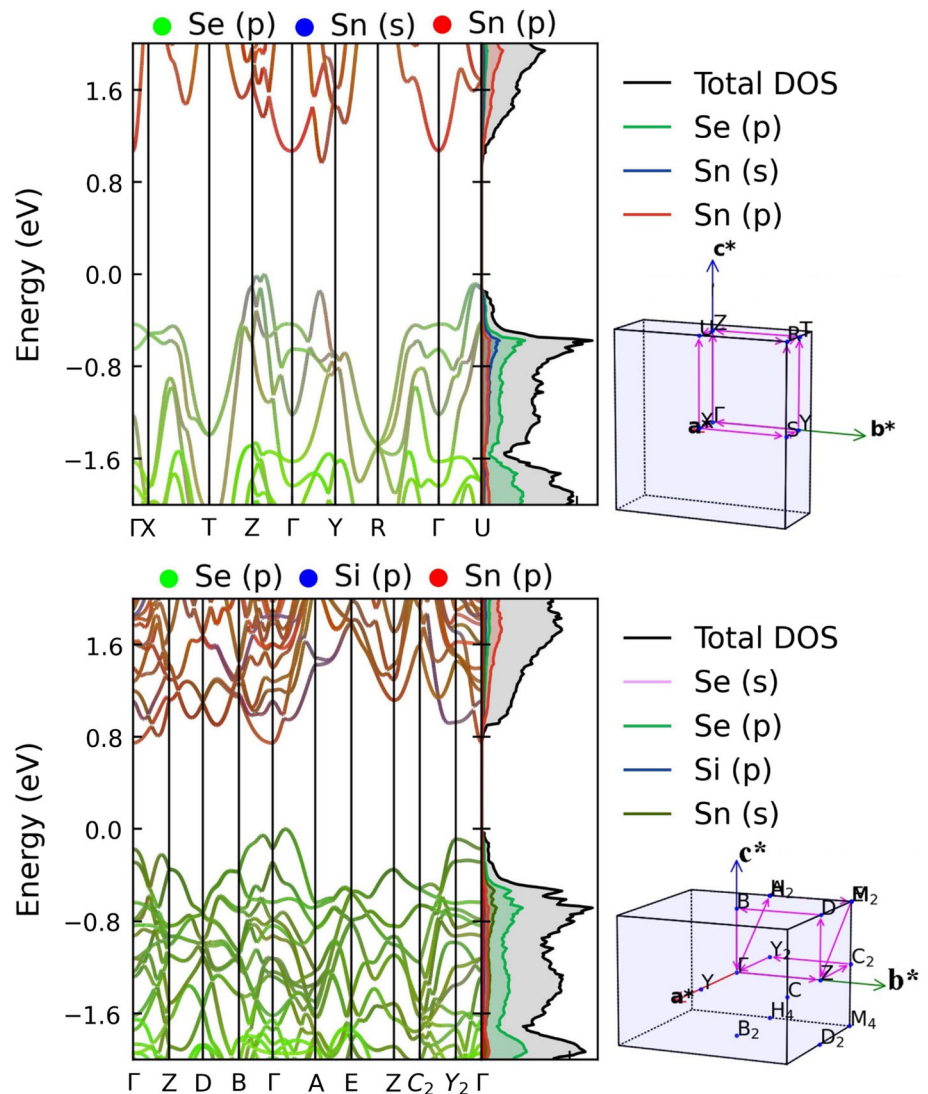


Table 1 The DFT-obtained results of the electronic bandgap energies for the pristine and Si-alloyed α -SnSe

Bandgap (eV) with different Functionals	PBE	SCAN	MBJ	G_0W_0	HSE06	BSE	Exp	Theory
α -SnSe	0.56	0.75	0.96	0.99	0.88	0.90	0.86 ^a 0.92 ^b	0.61 ^a 0.935 ^c
$\text{Si}_{0.0625}\text{Sn}_{0.9375}\text{Se}$	0.42	0.63	0.74	0.89	0.853	0.89	—	—
$\text{Si}_{0.125}\text{Sn}_{0.875}\text{Se}$	0.47	0.72	0.83	0.91	0.884	0.92	—	—
$\text{Si}_{0.1875}\text{Sn}_{0.8125}\text{Se}$	0.50	0.68	0.78	0.97	0.917	0.95	—	—
$\text{Si}_{0.25}\text{Sn}_{0.75}\text{Se}$	0.49	0.65	0.75	0.94	0.924	0.97	—	—

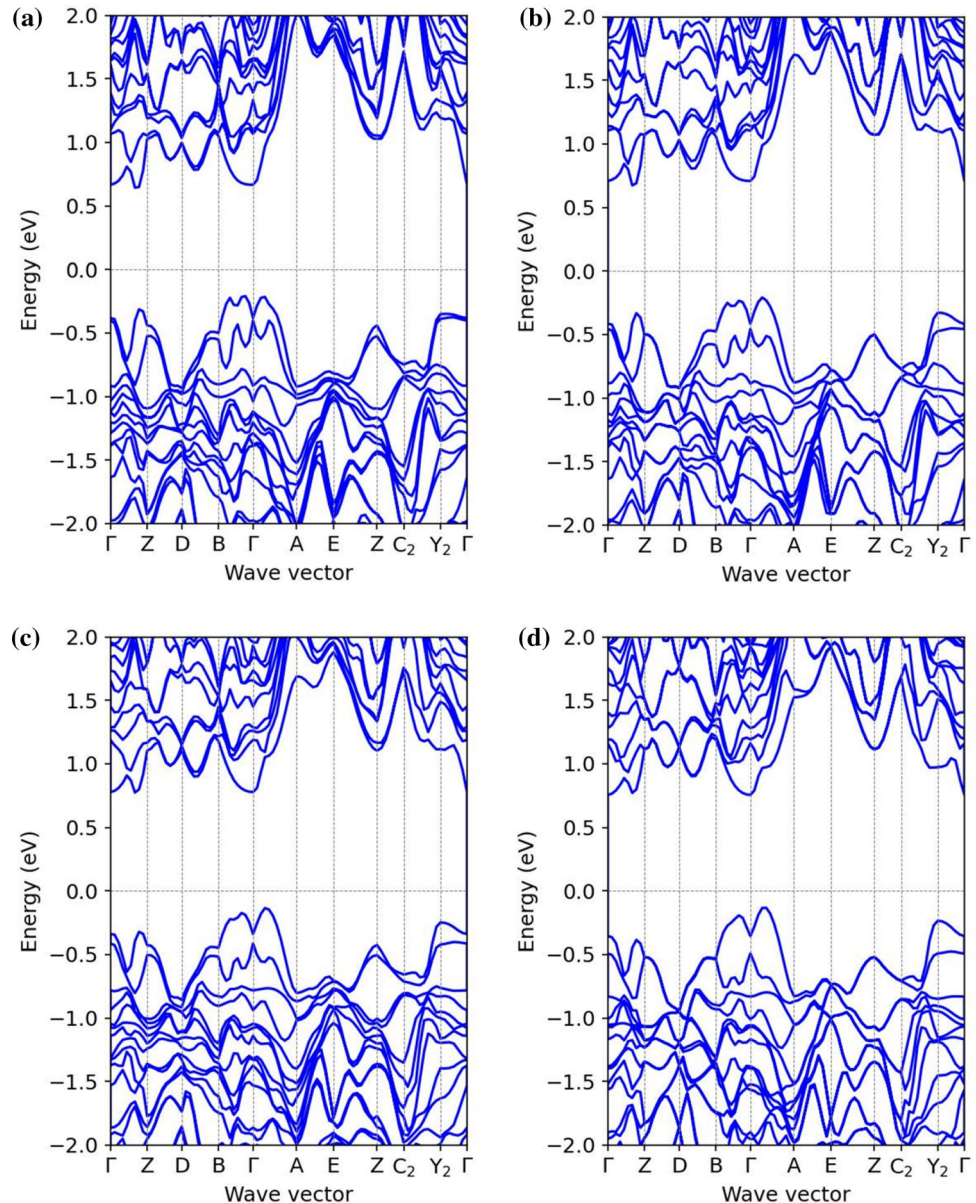
The calculations were done using different functionals compared with experimental reports and other theoretical studies

^aRef. [29], ^bRef. [24], ^cRef [55]

the Si concentration in $\text{Si}_x\text{Sn}_{1-x}\text{Se}$ alloys, the bandgap slightly increases. But only the 6.25% Si-alloying bandgap reduces by 3%.

From the DOS plot analysis shown in Fig. 4, it can be seen that the p -states of Se dominate in the valence band region. In contrast, the p -states of Sn are contributed more to the conduction band, which has

Figure 3 Electronic band structure of the pristine Si-alloyed α -SnSe **a** $\text{Si}_{0.0625}\text{Sn}_{0.9375}\text{Se}$, **b** $\text{Si}_{0.125}\text{Sn}_{0.875}\text{Se}$, **c** $\text{Si}_{0.1875}\text{Sn}_{0.8125}\text{Se}$, and **d** $\text{Si}_{0.25}\text{Sn}_{0.75}\text{Se}$ calculated using the DFT with HSE06 functional.



been attributed to the discrepancy in electronegativity as explained above. Although the contribution of Si atom increases in $\text{Si}_x\text{Sn}_{1-x}\text{Se}$ materials by the increase of Si content, Fig. 4 shows the small contribution of Si (s , p states) in the electronic DOS plot in the energy regime of Fermi level. Si dopant's s - and p -states exist in the same energy region of the Sn atoms. As a result, Si cannot efficiently boost valence band energy [63]. In most energy domains shown in Fig. 4, s - and p -states of Si display DOS compatibility with the s -states of Sn. Around the Fermi energy, the s - and p -states of Sn were hybridized with Se p -states to form peaks as well as both s - and p -states of Si also got hybridized with Sn s -states to contribute to total

DOS. As shown in Fig. 4, increasing the Si content in $\text{Si}_x\text{Sn}_{1-x}\text{Se}$ alloys (namely, $x = 6.25\%$, 12.5% , 18.75% , and 25%) does not affect the overall shape of the valence and conduction bands. Se p -states dominate the valence band, while the Si contribution remains minimal.

Optical properties

In this part, the optical properties of the $\text{Si}_x\text{Sn}_{1-x}\text{Se}$ are explored for their enormous potential in optoelectronics. Investigating a Si-alloyed α -SnSe material's optical properties is essential for understanding its features for optoelectronic applications. Optical

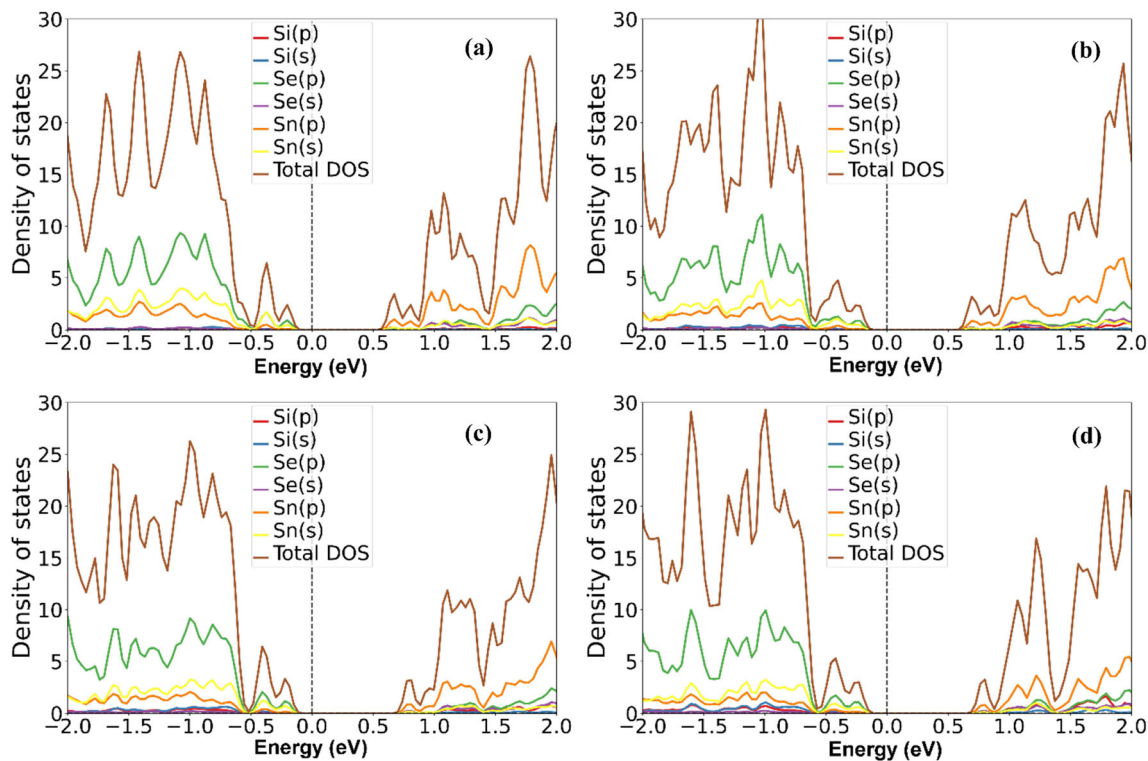


Figure 4 Density of states plots of the pristine Si-alloyed α -SnSe **a** $\text{Si}_{0.0625}\text{Sn}_{0.9375}\text{Se}$, **b** $\text{Si}_{0.125}\text{Sn}_{0.875}\text{Se}$, **c** $\text{Si}_{0.1875}\text{Sn}_{0.8125}\text{Se}$, and **d** $\text{Si}_{0.25}\text{Sn}_{0.75}\text{Se}$ calculated using DFT with the HSE06 functional.

properties explain how a substance behaves when subjected to electromagnetic radiation. The α -SnSe is a potential material of relevance for optoelectronics and photovoltaic applications because of its narrow bandgap and high optical absorption coefficient ($\sim 10^5/\text{cm}$). The optical spectra of the $\text{Si}_x\text{Sn}_{1-x}\text{Se}$ materials are obtained using random phase approximation (RPA) and solving the Bethe–Salpeter equation starting from the $G_0W_0(G_0W_0+\text{RPA})$ approximation because of its accurate optical outcomes close to experimental data, although these calculations are computationally costly. The G_0W_0 calculations solely consider electron–electron interactions, but the G_0W_0 plus BSE calculations consider both electron–electron(e–e) and electron–hole(e–h) interactions. Several prior investigations have demonstrated that excitonic effects contribution from e–h interactions accurately describes optical spectra [64, 65].

Optical properties of the pristine and Si-alloyed α -SnSe can be represented by the real component $\varepsilon_1(\omega)$ and imaginary part $\varepsilon_2(\omega)$ of the dielectric function, and the derivation procedure can be found in our prior study [55]. Figure 5 presents the absorption coefficient “ $\alpha(\omega)$ ”, refractive index “ $n(\omega)$ ”, reflectivity

“ $R(\omega)$ ”, and extinction coefficient “ $K(\omega)$ ” for the $\text{Si}_x\text{Sn}_{1-x}\text{Se}$ materials (where $x = 0, 6.25\%, 12.5\%, 18.75\%$, and 25%). Only the average of the anisotropic contributions from the a , b , and c directions is shown. We have presented the visible light area from 1.8 eV to 3.2 eV in the optical spectra of $\text{Si}_x\text{Sn}_{1-x}\text{Se}$ alloys (Fig. 5).

One can observe from Fig. 5 that the absorption edge (optical gap) calculated at the level of $G_0W_0+\text{BSE}$ approximation of the α -SnSe, $\text{Si}_{0.0625}\text{Sn}_{0.9375}\text{Se}$, $\text{Si}_{0.125}\text{Sn}_{0.875}\text{Se}$, $\text{Si}_{0.1875}\text{Sn}_{0.8125}\text{Se}$, and $\text{Si}_{0.25}\text{Sn}_{0.75}\text{Se}$ start from the energy values 1.01, 0.89, 0.92, 0.95, and 0.97, respectively. From Table 1, it can be noted that for the undoped α -SnSe, the quasi-particle optical gap (G_0W_0) is found to be 0.99, which is slightly higher than the experimental gap of 0.86 eV [29] without considering the e–h interactions. When e–h interactions are included with $G_0W_0+\text{BSE}$ approaches, the optical gap of 0.90 eV is very close to the experimental optical bandgap. It can be seen from Fig. 5a that for all the Si-alloyed $\text{Si}_x\text{Sn}_{1-x}\text{Se}$ alloys, the peaks lie in the visible region. Also, it can be visualized that with the increasing Si concentration, the peaks are much higher than the undoped SnSe in the

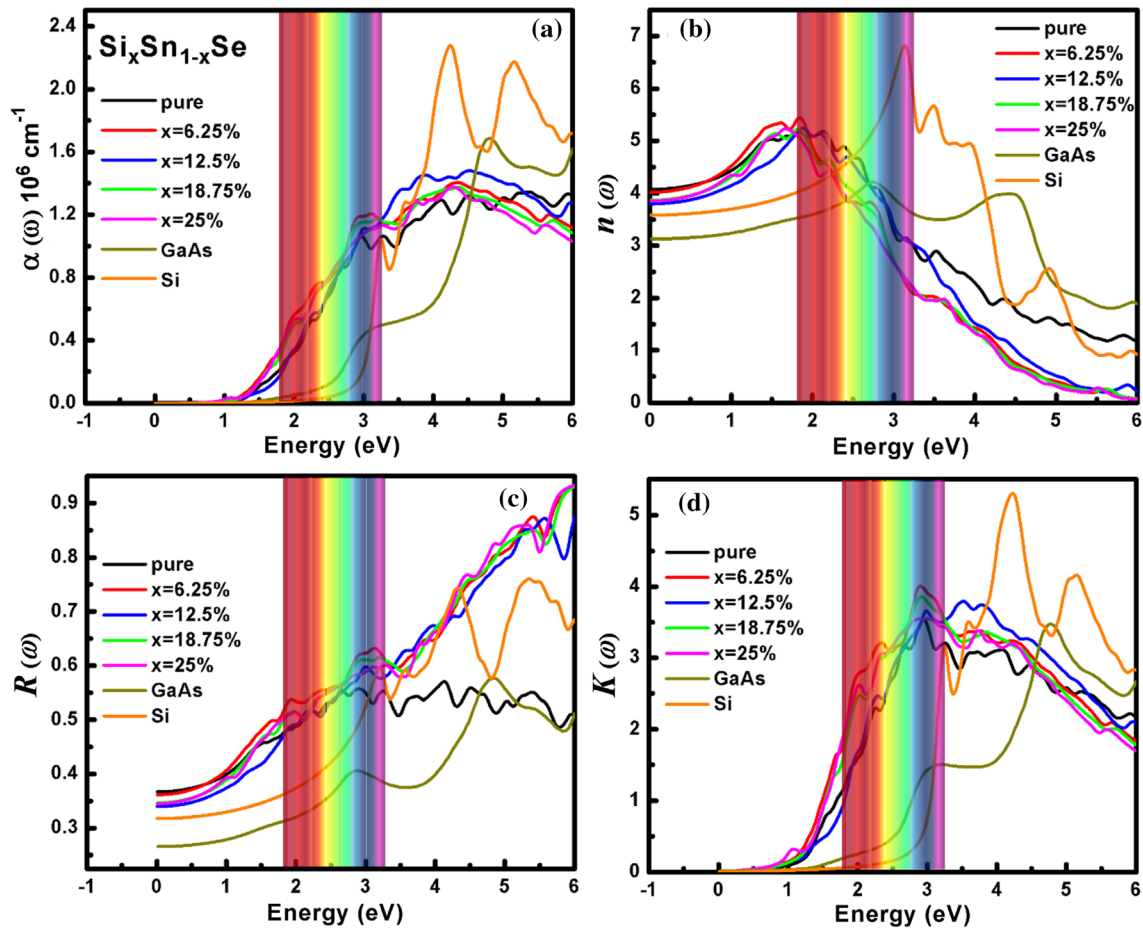


Figure 5 **a** absorption coefficient: $\alpha(\omega)$, **b** refractive index: $n(\omega)$, **c** reflectivity: $R(\omega)$, and **d** extinction coefficient: $K(\omega)$ for the $\text{Si}_x\text{Sn}_{1-x}\text{Se}$ materials (for $x = 0, 6.25\%, 12.5\%, 18.75\%$, and 25%) calculated with BSE level at the top of G_0W_0 approximation.

visible area. Figure 5a shows that Si-alloying improves SnSe light absorption at $x = 0.0625$ with high peaks of $\sim 1.2 \times 10^6 \text{ cm}^{-1}$ concentrated in the visible light region. The Si-alloyed α -SnSe with $x = 0.125$, on the other hand, has lower light absorption in the visible area but increases it in the ultraviolet (UV) region, notably at energy levels of about 4.5 eV. For a wide range of energy levels, the higher concentration of Si doping (at $x = 0.1875, 0.25$) materials show nearly equal scattering peaks but are higher than the undoped SnSe.

Light harvesting ability of Si-alloyed SnSe has been compared to that of typical optoelectronic materials like GaAs and Si. Figure 5a shows, for instance, the optical absorption coefficient of Si and GaAs computed at the G_0W_0 -BSE level, together with the $\text{Si}_x\text{Sn}_{1-x}\text{Se}$ alloys. Si, GaAs, and the Si-alloyed SnSe all show noticeable peaks between 3 and 6 eV in energy range. It shows that both Si and GaAs absorb both

visible and very intense UV radiation. In the visible light spectrum, Si-alloyed SnSe has higher peaks than Si and GaAs, whereas in the ultraviolet spectrum, Si and GaAs have substantially higher absorption peaks than $\text{Si}_x\text{Sn}_{1-x}\text{Se}$ alloys. $\text{Si}_x\text{Sn}_{1-x}\text{Se}$ alloys likewise Si, and GaAs show quite high absorption ($\sim 10^6 \text{ cm}^{-1}$) which is promising. The Si-alloyed SnSe systems can be considered as good solar energy absorbers in the visible light spectrum.

Furthermore, Si-alloyed SnSe exhibits the semi-conducting property in accordance with the band structure and DOS plots in Figs. 3 and 4, respectively. The excited electrons in the undoped and Si-alloyed systems transit from occupied to unoccupied states due to the Se- p and Si- s states, respectively. For all the $\text{Si}_x\text{Sn}_{1-x}\text{Se}$ materials, there is a rapid increase in the absorption spectra after the bandgap, indicating solid optical absorption and implying that greater photocurrent may be produced for the investigated

materials. Si-alloying improves the light absorption of SnSe and reaches a maximum of $\sim 1.5 \times 10^6 \text{ cm}^{-1}$ for a wide energy range from visible to ultraviolet. $\text{Si}_x\text{Sn}_{1-x}\text{Se}$ is capable of absorbing a broader spectrum of electromagnetic wavelengths. It is widely perceived that a broad absorption spectrum, particularly in the infrared region, can boost the efficiency in converting solar energy toward renewable energy.

The refractive index " $n(x)$ " as a function of photon energy for the $\text{Si}_x\text{Sn}_{1-x}\text{Se}$ alloys is provided in Fig. 5b. The anisotropic average of the static refractive index " $n(0)$ " for the undoped SnSe is found to be 4.07, which decreases with the increasing Si concentration. For the $\text{Si}_x\text{Sn}_{1-x}\text{Se}$ at $x = 0.25$, the value of the static refractive function is observed at 3.84. It can be observed that Si-alloying can be used to lower the static refractive index, and it has only a minor influence on the static refractive index spectra of $\text{Si}_x\text{Sn}_{1-x}\text{Se}$ alloys. The highest peak is found for the $\text{Si}_x\text{Sn}_{1-x}\text{Se}$ at $x = 0.0625$ and is located at the commencement of the visible region. For all the studied materials, refractive index spectra begin to drop after passing into the visual part, although they stay positive. Figure 5b also compares the refractive index as a function of incident photon energy for Si-alloyed SnSe and Si, GaAs. GaAs have a refractive index of $n = 3.9$ at 2.76 eV, which is very close to the experimental value of 3.59. At 3.15 eV, the refraction index of Si reaches its maximum value of 6.79. The static refractive index of $\text{Si}_x\text{Sn}_{1-x}\text{Se}$ can be seen to be higher than that of pure Si and GaAs. For $\text{Si}_x\text{Sn}_{1-x}\text{Se}$ alloys, the index of refraction moves to a region with less energy, which causes the red-shifting effect.

The reflectivity " $R(\omega)$ " of solids is defined by the difference in transmitted and reflected power. Figure 5c presents the measured plots of $R(\omega)$ for the $\text{Si}_x\text{Sn}_{1-x}\text{Se}$ alloys. The Si-alloyed systems have a lower value of the static reflectivity $R(0)$ than the undoped SnSe. Compared to the undoped system, the Si-alloyed SnSe alloys have a slight lift in the reflection peaks. In the visible area, the Si-alloyed alloys reflect more and are more prominent than the undoped system. The reflectance of α -SnSe systems is high until the visible area and remains almost constant in the ultraviolet region. In contrast, a steep increase can be seen in Si-alloyed systems' reflectance throughout the photon energy region. Figure 5c depicts the reflectivity spectrum of $\text{Si}_x\text{Sn}_{1-x}\text{Se}$ alloys in addition to GaAs and Si. The less reflective a

material is, the more photons hit the material's surface, which can reduce energy loss and cause more photoelectrons to form. Figure 5c demonstrates that the reflectivity peaks of $\text{Si}_x\text{Sn}_{1-x}\text{Se}$ are more significant than those of Si and GaAs across the entire energy spectrum. However, the Si reflectivity peak is lower than that of GaAs and Si-alloyed SnSe, indicating that the extremely low reflectivity is primarily attributable to Si's exceptional light-trapping properties.

The extinction coefficient $K(\omega)$ as a function of photon energy for the $\text{Si}_x\text{Sn}_{1-x}\text{Se}$ alloys investigated is shown in Fig. 5d. The static extinction coefficient $K(0)$ value is moderately negligible for all of the DFT-studied systems. The value of extinction coefficient $K(\omega)$ begins to increase once the corresponding bandgap values of the pure and Si-alloyed -SnSe systems are reached. At $x = 0.0625$, the highest $K(\omega)$ value is found to be about ~ 4 for $\text{Si}_x\text{Sn}_{1-x}\text{Se}$. Figure 5d shows that the global peak of the extinction coefficient $K(\omega)$ falls in the visible light range for all Si-alloyed systems, indicating significant absorption and short-path transmission of visible light $\text{Si}_x\text{Sn}_{1-x}\text{Se}$ alloys.

Mechanical properties

Elastic constants are key mechanical parameters for crystal structures that indicate the mechanical response of the materials to external forces and stresses. We have calculated the elastic constants to check the mechanical stability of the $\text{Si}_x\text{Sn}_{1-x}\text{Se}$ materials. According to Hooke's law, a crystal's applied stress (σ_i) is proportional to the resulting strain (ϵ_j) within a defined elastic regime.

$$\sigma_i = \sum C_{ij} \epsilon_j \quad (1)$$

where C_{ij} is the tensor of elastic constant that predicts the structure stability by measuring the response of the crystal lattice to the exterior forces and giving information about the binding nature of the adjacent atomic planes and the anisotropic character of the bonds. Elastic constants (C_{ij}) of any material signify the measure of stiffness for a distinct crystal structure deformation.

Table 2 shows the computed elastic constants of orthorhombic α -SnSe and monoclinic $\text{Si}_x\text{Sn}_{1-x}\text{Se}$ (where $x = 6.25\%$, 12.5% , 18.75% , and 25%) alloys. Our DFT investigated pristine α -SnSe and Si-alloyed $\text{Si}_x\text{Sn}_{1-x}\text{Se}$ materials. These structures are

mechanically stable since their computed elastic constants meet Born’s mechanical stability criteria [66]. The stiffness to uniaxial stresses along the crystallographic axes *a*, *b*, and *c* is represented by C_{11} , C_{22} , and C_{33} , respectively. Along these axes, C_{22} has the greatest value, as shown in Table 2, and C_{33} is the lowest, revealing that SnSe is stiffest for strains in the *b*-direction and softest for strains in the *c*-direction. In Table 2, we have compared our DFT-calculated elastic constants of α -SnSe with other theoretical and experimental data. Table 2 shows that the lattice constant of α -SnSe calculated using DFT agrees well with other theoretical [67] and experimental data. We can see that C_{11} and C_{33} are marginally smaller when compared to the bulk black phosphorus [54], but C_{22} of black phosphorus is twice larger than that of SnSe, indicating that SnSe is significantly softer than black phosphorus along the *b*-direction, even though they have a similar crystal lattice.

Other elastic moduli can be determined using the calculated elastic constants (C_{ij}). For the orthorhombic α -SnSe and monoclinic $Si_xSn_{1-x}Se$ (where $x = 6.25\%$, 12.5% , 18.75% , and 25%) alloys, the bulk and shear moduli of Voigt and Reuss are determined by using Ref. [68]. The upper and lower limit of the polycrystalline constants is represented by the relations of Voigt and Reuss, respectively. Hence, Hill’s approximation is used to calculate these moduli. The averages of the Voigt and Reuss bounds are

computed using the Voigt–Reuss–Hill approximations [69] as:

$$B_{VRH} = \frac{B_V + B_R}{2}, \quad G_{VRH} = \frac{G_V + G_R}{2} \tag{2}$$

The Young’s modulus (E) and the Poisson’s ratio (ν) can be obtained from the following relation:

$$E = \frac{9BG}{3B + G}, \quad \nu = \frac{3B - 2G}{2(3B + G)} \tag{3}$$

Our DFT-obtained values of the bulk, shear, and Young’s moduli, as well as Poisson’s ratio derived from the above equations, are listed in Table 3, which agree well with other theoretical [32, 67] [67, 70] and experimental [54] values. The ductility index (B/G) describes the toughness or fracture of the polycrystalline material, and its corresponding low(high) value of the B/G ratio should reveal the brittleness/ductility of the material. Generally, ductile materials have a B/G proportion greater than 1.75, while brittle materials have a B/G less than 1.75 [67]. The ductility index (B/G) values of pristine and Si-alloyed α -SnSe materials presented in Table 3 indicate that all the studied materials in this work are brittle. Moreover, our DFT-obtained bulk modulus (B) and shear modulus (G) were used to calculate the longitudinal (v_l) and shear (v_s) wave velocities as follows [71]:

Table 2 DFT-calculated elastic stiffness constants C_{ij} (GPa) for the orthorhombic α -SnSe and monoclinic $Si_xSn_{1-x}Se$ alloys

C_{ij} (GPa)	α -SnSe			$Si_xSn_{1-x}Se$			
	This work	Other DFT ^a	Experimental ^b	at $x = 6.25\%$	at $x = 12.5\%$	at $x = 18.75\%$	at $x = 25\%$
C_{11}	44.12	41.1	41.8	30.85	29.46	30.10	30.18
C_{22}	65.99	65.7	59.7	66.23	65.93	66.61	68.41
C_{33}	34.87	29.6	32.5	45.35	45.99	46.39	48.68
C_{44}	13.11	12.0	13.2	13.62	14.36	15.33	18.02
C_{55}	28.50	29.6	24.5	14.47	15.31	16.39	18.80
C_{66}	16.62	14.7	20.5	28.95	28.84	29.74	29.33
C_{12}	8.45	7.33	3.15	27.59	25.97	26.59	25.18
C_{13}	13.43	12.1	10.7	12.98	13.47	13.90	16.36
C_{23}	29.84	26.9	26.8	9.02	9.13	9.87	12.22
C_{15}	–	–	–	– 0.16	– 0.54	– 0.40	– 0.82
C_{25}	–	–	–	0.32	1.06	1.46	2.27
C_{35}	–	–	–	0.26	0.40	0.37	– 0.13
C_{46}	–	–	–	0.53	0.83	2.18	3.36

^aRef. [67], ^bRef [54]

Table 3 Elastic moduli: Bulk Modulus (B), Shear Modulus (G), Young's Modulus (E), Poisson's Ratio (ν), and Ductility Index (B/G) along with the values of longitudinal wave velocity (v_l), shear wave

velocity (v_s), average sound velocity (v_m), and Debye temperature (θ_D) of the pristine and Si-alloyed α -SnSe

Elastic Parameters	α -SnSe			$\text{Si}_x\text{Sn}_{1-x}\text{Se}$			
	This work	Other DFT ^a	Experimental ^b	$x = 6.25\%$	$x = 12.5\%$	$x = 18.75\%$	$x = 25\%$
B (GPa)	23.53	24.1	23.2	25.52	25.22	25.74	26.94
G (GPa)	14.86	15.2	16.0	15.68	15.97	16.44	17.43
E (GPa)	33.87	37.6	39.0	39.05	39.57	40.66	43.01
ν	0.287	0.24	0.22	0.245	0.238	0.236	0.233
B/G	1.58	1.59	1.45	1.62	1.57	1.56	1.54
v_l (m/s)	2750	2711	2717	2840	2870	2930	3030
v_s (m/s)	1510	1587	1629	1650	1680	1720	1780
v_m (m/s)	1670	1759	1803	1830	1870	1910	1980

^aRef. [67], ^bRef [54]

$$v_l = \sqrt{\frac{B + 4G/3}{\rho}}, \quad v_s = \sqrt{\frac{G}{\rho}} \quad (4)$$

and the average sound velocity can be deduced from Eq. 4 as:

$$v_m = \left[\frac{1}{3} \left(\frac{2}{V_l^3} + \frac{1}{V_s^3} \right) \right]^{-1/3} \quad (5)$$

From Table 3, it can be noted that our obtained values of the pristine α -SnSe longitudinal (v_l), shear (v_s), and average (v_m) sound wave velocities agree well with other DFT [67] and experimental work [54]. To the best of our knowledge, no theoretical or experimental data is available on the elastic moduli of Si-alloyed α -SnSe to compare with.

Vibrational properties

The vibrations of phonon modes for the $\text{Si}_x\text{Sn}_{1-x}\text{Se}$ alloy were simulated using DFT calculations, which can help understand the inherent explanation for the low lattice thermal conductivity and elucidate the basic concepts of lattice dynamics. Figure 6a and b shows our DFT-calculated phonon dispersion bands, total phonon DOS, and projected phonon DOS for the pristine α -SnSe, respectively. The phonon dispersion of the pristine α -SnSe has no imaginary frequency, as shown in Fig. 6, indicating its vibrational stability. It also features a bipartite structure divided into two groups, each with twelve phonon branches. The distorted variation of a diatomic NaCl composition

can be attributed to the primitive unit cell of α -SnSe (Pnma) [29]. SnSe is compatible with a bipartite spectrum as it is lower (upper) half corresponds to the NaCl unit cell's folded acoustic (optical) modes [58]. Another conclusion from this line of reasoning is that sound velocity should be nearly isotropic. Acoustic modes along the Γ -Y K-path are much softer than those along with the Γ -Y and Γ -Z K-path directions, as seen in Fig. 6a. Such soft modes in pristine α -SnSe suggest that strong anharmonicity and weak interatomic bonding are possible [29]. Due to soft-mode lattice instability, which occurs from the synchronization of Se p -states with stereochemically Sn lone pair, the phonons in α -SnSe are very anisotropic. The Jahn–Teller electronic instability of α -SnSe, driven by its lattice distortion, is resulting in a considerable anharmonicity [68].

Figures 7 and 8 show the phonon dispersions, phonon DOS, and the projected phonon DOS for the $\text{Si}_x\text{Sn}_{1-x}\text{Se}$ materials (where $x = 6.25\%$, 12.5% , 18.75% , and 25%), respectively. The phonon dispersion curve shows no imaginary frequencies for all the Si-alloyed studied materials, indicating that the Si-alloyed α -SnSe structures are thermodynamically stable. From Fig. 9, analyzing the projected DOS of $\text{Si}_x\text{Sn}_{1-x}\text{Se}$ reveals that the optical branches of $\text{Si}_x\text{Sn}_{1-x}\text{Se}$ have a greater energy eigenvalue than pristine α -SnSe, which is attributed to the lighter atomic mass of Si. The lighter Si contributes to the high-frequency modes, whereas the heavier Sn and Se elements contribute to the low-frequency modes. On the other hand, the optical phonon branches are

Figure 6 Calculated **a** phonon dispersion curve along the high-symmetry lines of Brillouin zone; **b** total and projected phonon density of states for the pristine α -SnSe.

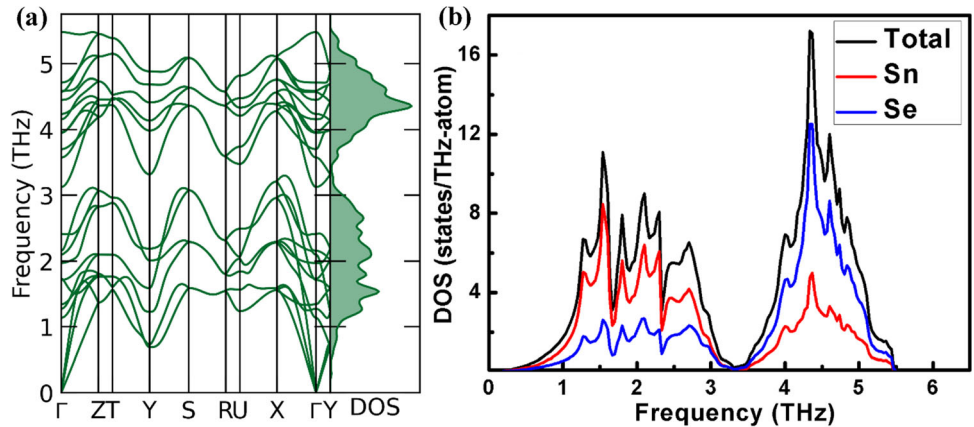
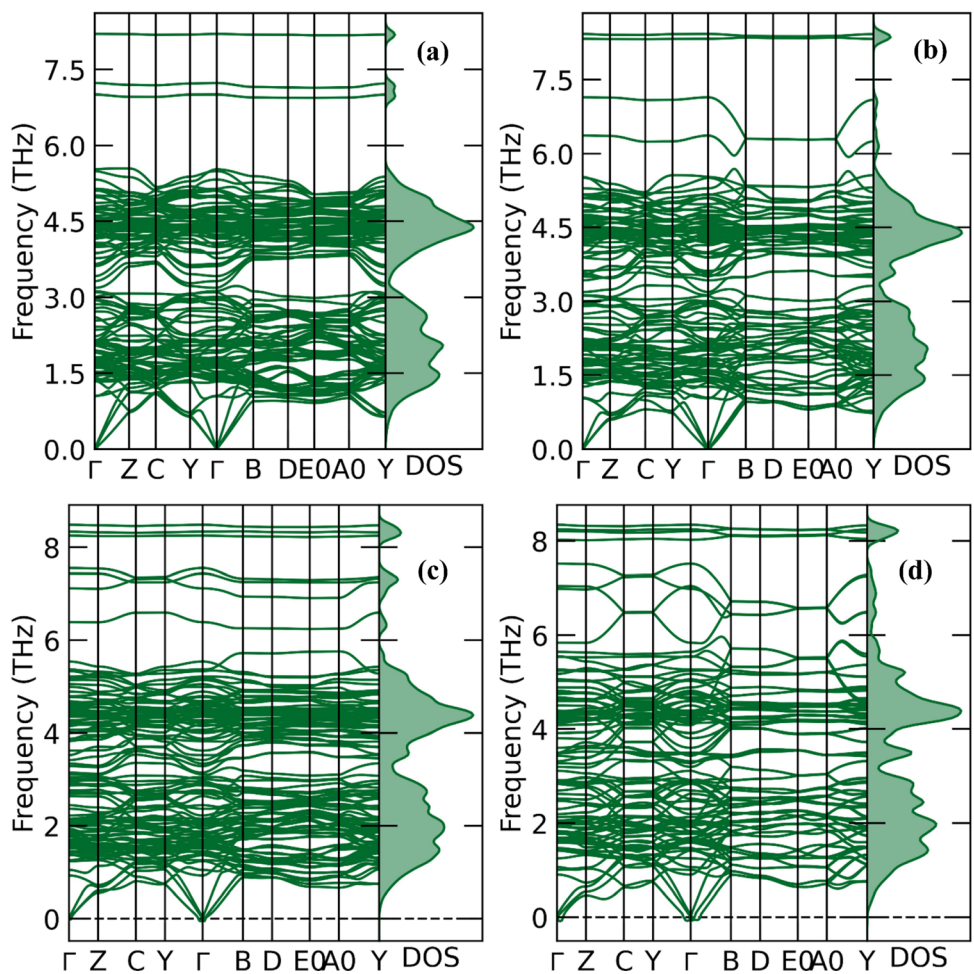


Figure 7 Calculated phonon dispersion bands along the high-symmetry lines of Brillouin zone, for the **a** $\text{Si}_{0.0625}\text{Sn}_{0.9375}\text{Se}$, **b** $\text{Si}_{0.125}\text{Sn}_{0.875}\text{Se}$, **c** $\text{Si}_{0.1875}\text{Sn}_{0.8125}\text{Se}$, and **d** $\text{Si}_{0.25}\text{Sn}_{0.75}\text{Se}$.



relatively flat in the Γ -Y direction (*a*-axis), indicating a low phonon frequency and ascribed to weak interactions between adjacent SnSe layers. It can be seen from Fig. 8 that the phonon branches for acoustic and optical phonons are shifted down, resulting in lesser phonon dispersion and lower phonon frequency. Figures 6a and 7 show the lower

group velocities of optical phonons and softening acoustic modes. Despite the appearance of multiple bands in Fig. 7, the group velocities of the optical and acoustic phonons barely alter in the $-X$ -direction. Instead, the acoustic phonons are retarded in the Γ -Y, and Γ -Z directions. Thus, the Si substitution mostly affects the *b* and *c* axes rather than the *a*-axis.

Figure 8 Projected phonon density of states for the Si-alloyed α -SnSe systems. **a** $\text{Si}_{0.0625}\text{Sn}_{0.9375}\text{Se}$, **b** $\text{Si}_{0.125}\text{Sn}_{0.875}\text{Se}$, **c** $\text{Si}_{0.1875}\text{Sn}_{0.8125}\text{Se}$, and **d** $\text{Si}_{0.25}\text{Sn}_{0.75}\text{Se}$.

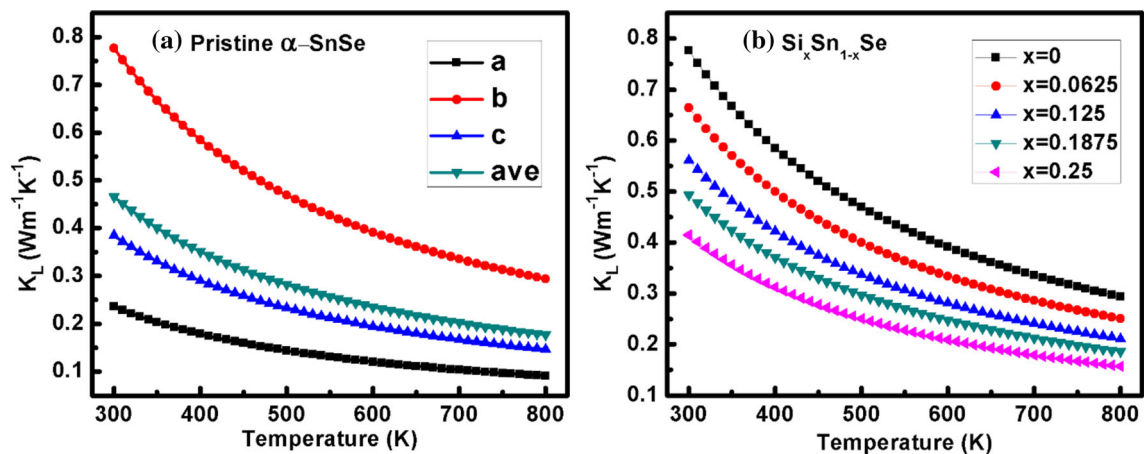
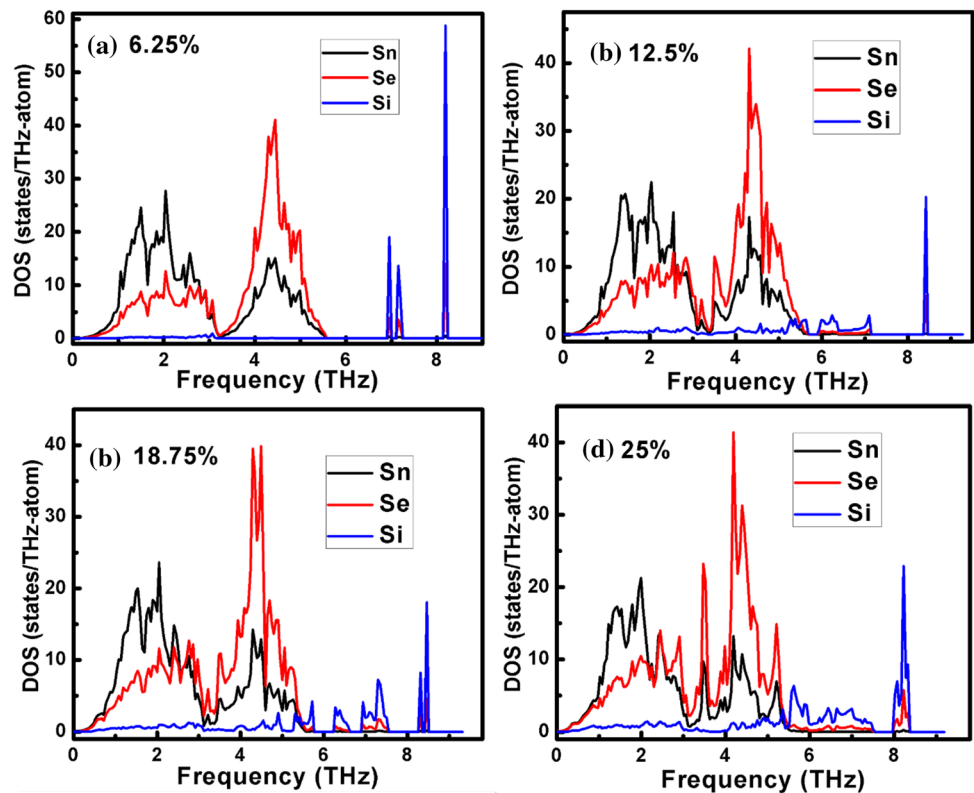


Figure 9 Lattice thermal conductivity of the **a** pristine α -SnSe along the a , b , and c -direction and **b** lattice thermal conductivity along the b -direction for $\text{Si}_x\text{Sn}_{1-x}\text{Se}$ ($x = 0, 6.25\%, 12.5\%, 18.75\%$, and 25%).

A comparison of the phonon lifetime versus phonon frequency plots between the pristine and Si-alloyed SnSe systems is presented in the supplementary Figure S3. It can be observed that Si-alloyed systems do possess shorter phonon lifetime especially for the higher Si concentrations of 18.75% and 25%, as shown in the supplementary Figure S3 (d, e), suggesting the stronger phonon scattering (lower phonon lifetime).

Thermoelectric properties

In solids, electrons and lattice vibrations are primarily responsible for thermal conductivity. The lattice vibrations (κ_l) through phonons and the electronic contribution (κ_e) contribute to the total thermal conductivity $\kappa = \kappa_l + \kappa_e$. The κ_l leads the thermal conductivity in case of semiconductors, whereas κ_e comes out on top in case of metallic compounds. We

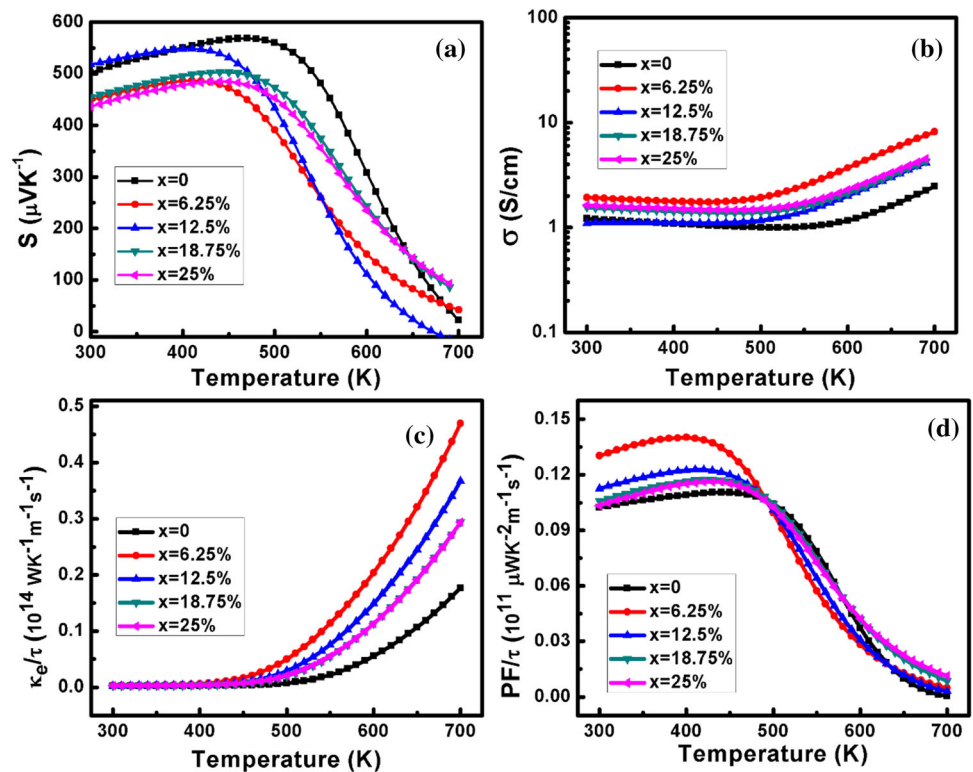
used phonon transport simulations to calculate and understand the process for lowering the lattice thermal conductivity by Si doping in α -SnSe. Figure 9a and b presents our calculated temperature-dependent lattice thermal conductivity values for the single-crystal α -SnSe, and Si-alloyed $\text{Si}_x\text{Sn}_{1-x}\text{Se}$ alloys, respectively. For a crystalline material, SnSe has the lowest value of the lattice thermal conductivity [58] because of the large number of optical modes and low frequency. Due to the layered crystal lattice of both pristine α -SnSe and $\text{Si}_x\text{Sn}_{1-x}\text{Se}$ alloys, lattice thermal conductivity is significantly smaller along the a -axis than along the b - and c -axes, making it anisotropic. Our calculated values of the lattice thermal conductivity for α -SnSe are 0.23, 0.77, and 0.38 (in $\text{Wm}^{-1}\text{K}^{-1}$) at 300 K, which are in reasonable agreement with the experimental values of ~ 0.46 , 0.70, and 0.68 along the three a -, b - and c -directions, respectively [29]. Notably, at room temperature, along the b -axis, κ_1 matches well with the experimental value and other theoretical values $\kappa_1^b = 0.70\text{Wm}^{-1}\text{K}^{-1}$ [29]. In contrast, κ_1 for the two different directions (along the a - & c -axis) differ significantly. As α -SnSe presents the highest thermoelectric performance along the b -axis, we have shown the lattice thermal conductivity for the $\text{Si}_x\text{Sn}_{1-x}\text{Se}$ alloys only along the b -axis in Fig. 9b. The lattice thermal conductivity of the $\text{Si}_x\text{Sn}_{1-x}\text{Se}$ alloys also follows the strong axial anisotropy as that of α -SnSe, i.e., $\kappa_1^a < \kappa_1^c < \kappa_1^b$ at the entire temperature range. Our theoretically predicted lattice thermal conductivity of the Si-alloyed α -SnSe shows the lower values for all the temperature ranges with increasing Si content than that of the pristine α -SnSe. At the high temperature of 770 K, the value of κ_1 for the α -SnSe is found to be $\sim 0.30\text{Wm}^{-1}\text{K}^{-1}$ which is in excellent agreement with other DFT-calculated values of $\sim 0.36\text{Wm}^{-1}\text{K}^{-1}$ [29]. All the Si-alloyed samples show the decreasing trend by increasing temperature, and their lattice thermal conductivity was significantly reduced to $\sim 0.2\text{Wm}^{-1}\text{K}^{-1}$ at the 770 K due to the phonon scattering mechanism. The influence of the lighter Si atom on the κ_1 is minor, implying that the crystal structure difference, particularly the weak Sn–Si bonds, plays a significant role in the changed lattice vibration and phonon scattering that occurs when SnSe is replaced by Si ions. At 770 K, $\text{Si}_x\text{Sn}_{1-x}\text{Se}$ material has the lowest thermal conductivity of $\sim 0.16\text{Wm}^{-1}\text{K}^{-1}$ at the $x = 0.25$. Experimentally, the

pristine α -SnSe has the lowest value of ~ 0.20 – $0.34\text{Wm}^{-1}\text{K}^{-1}$ at 973 K [29].

The α -SnSe single crystal is a p -type semiconductor with holes as the primary charge carriers. The temperature-dependent thermoelectric properties are presented in Fig. 10 from 300 to 700 K. We have selected the fixed carrier concentration $6 \times 10^{-17}\text{cm}^{-3}$ for all the systems extracted from the Hall coefficient measurements [29]. The calculated values of the Seebeck coefficient for the pristine α -SnSe, and $\text{Si}_x\text{Sn}_{1-x}\text{Se}$ alloys as a function of temperature are shown in Fig. 10a. At room temperature, our calculated value of the Seebeck coefficient of 502.2 ($\mu\text{V}/\text{K}$) for the α -SnSe is in excellent agreement with the experimental value of 504.6 ($\mu\text{V}/\text{K}$) [72]. Figure 10a shows that the Si-alloyed system has lower Seebeck coefficient values in the entire temperature region than the pristine α -SnSe revealing the effort of Si substituting the position of Sn. The lower values of the Seebeck coefficient for the Si-alloyed systems can be attributed to the increased carrier concentration after significant Si alloying.

Firstly, the value of Seebeck coefficients starts increasing and reaches their maximal values around 450 K for the Si-alloyed systems, as shown in Fig. 10a. The maximum value of the Seebeck coefficient is 568 ($\mu\text{V}/\text{K}$) at 490 K and corresponds to the pristine α -SnSe and higher than those of the studied systems. After 490 K and ~ 450 K, the values of the Seebeck coefficient start decreasing for the pristine and Si-alloyed systems, respectively, due to the minority carrier excitation. The electrical thermal conductivity (σ) for $\text{Si}_x\text{Sn}_{1-x}\text{Se}$ alloys (where $x = 0$, 6.25%, 12.5%, 18.75%, and 25%) is presented in Fig. 10b. Electrical and thermal conductivity grows slowly with the increasing temperature for all the studied systems. After 500 K, it increases significantly due to the intrinsic excitation. In the entire temperature range, the Si-alloyed system has higher electrical conductivity values than the undoped α -SnSe. Figure 10c shows our DFT-calculated temperature-dependent electronic thermal conductivity for $\text{Si}_x\text{Sn}_{1-x}\text{Se}$ alloys (where $x = 0$, 6.25%, 12.5%, 18.75%, and 25%). Our determined values of electronic thermal conductivity follow the same pattern as electrical conductivity. Still, the values are extremely low, less than $0.05\text{Wm}^{-1}\text{K}^{-1}$ for all the studied systems across the whole temperature range. Figure 10d shows temperature-dependent Power factor (PF) for the

Figure 10 Temperature dependence plot of the measured properties **a** Seebeck coefficient “ S ” **b** electrical conductivity “ σ ” **c** electronic thermal conductivity “ κ_e ” and **d** power factor “PF” of the Si-alloyed α -SnSe.



$\text{Si}_x\text{Sn}_{1-x}\text{Se}$ systems (where $x = 0, 6.25\%, 12.5\%, 18.75\%$, and 25%). Figure 10d shows that the PF is slightly enhanced by increasing the Si concentration due to improved electrical conductivity, but for larger than ~ 450 K, PF starts decreasing for all the studied systems.

Conclusion

In summary, for the first time, we rigorously investigated the effect of Si-alloying on the structural, optoelectronic, mechanical, and thermoelectric properties of α -SnSe by using semi-classical Boltzmann transport theory combined with first-principles calculations. The electronic and thermoelectric properties of the pristine α -SnSe agree well with the experiment data. Throughout detailed structural and mechanical analysis, it is found that the morphology of the α -SnSe changes from the orthorhombic to monoclinic by Si-alloying. The bandgap reduction is very slight due to Si-alloying, and 6.25% content of Si is found to be adequate to lower the bandgap of α -SnSe by 0.03 eV calculated with HSE06 functional.

Optical properties of the $\text{Si}_x\text{Sn}_{1-x}\text{Se}$ alloys with Si-alloying calculated with the Bethe–Salpeter equation on the top of the non-self-consistent G_0W_0 approximations suggest an enhancement in the absorption, reflectivity, and extinction coefficient in the visible region of the electromagnetic spectra. Moreover, Si-dopants can effectively scatter the phonons and decrease the lattice thermal conductivity. Our DFT calculations revealed that Si-alloying in α -SnSe increases the electrical conductivity and the power factor. This research provides a deeper understanding of the optoelectronic and thermoelectric characteristics of SnSe good agreement with the available experimental and theoretical data.

Acknowledgements

The authors are indebted to thank the United Arab Emirates University Program for Advanced Research (UPAR) and the National Water and Energy Centre (NWEC) for their financial support under Grant Number 12R017.

Appendix: Effect of disorder on electronic structure

Our studied alloys seem to belong to the inhomogeneous category. Consequently, it becomes crucially important to elaborate a discussion about the effect of heterogeneity (i.e., disorder) on the electronic structure. We selected the case of $\text{Si}_x\text{Sn}_{1-x}\text{Se}$ alloys with $x = 0.125$, in which the computational supercell contains 2 Si atoms and 14 Sn atoms. Of course, the configurational space is so large as for instance in such simple case it contains: $C_{16}^2 = 120$ configurations. Among all these configurations, we selected 6 realizations attempting to take account of both clustering and homogenous alloys cases (i.e., when 2 Si atoms are either adjacent or farthest apart in either the same monolayer or different monolayers). The relaxed structures of the selected configurations are shown in Figure S1. We maintained the first Si atom stationary at substitutional position “a1”, while the second Si atom put at one of six different substitutional positions “b1–b6” as shown in Figure S1. The band structures corresponding to these six configurations are shown in Figure S2. Amazingly, the band structures are not far different. They all share in common by having the valence band maximum (VBM) located on ΓB high-symmetry line in the Brillouin zone, while the conduction band minimum (CBM) located on ΓZ high-symmetry line. The variation of bandgap energy is found to be ranging from 0.411 eV to 0.433 eV within a variance of about 22 meV. Furthermore, it is remarkable that the bandgap energies of the configurations of when the 2 Si atoms are adjacent in same monolayer and neighboring monolayer are 0.425 eV and 0.418 eV, respectively. These values lay in midrange of the interval of values. One more remark is that the largest bandgap is found to correspond to 2 Si atoms homogeneously distributed (i.e., at farthest distance apart) in same monolayer. All these trends are in support and can justify our use to the configurations of alloying one monolayer and carry on with the investigation of the optoelectronic and thermoelectric properties.

Supplementary Information: The online version contains supplementary material available at <http://doi.org/10.1007/s10853-022-07935-w>.

References

- [1] Siddique S, Gong Y, Abbas G et al (2022) Realizing high thermoelectric performance in p-Type SnSe crystals via convergence of multiple electronic valence bands. *ACS Appl Mater Interfaces* 14:4091–4099
- [2] He J, Kanatzidis MG, Dravid VP (2013) High performance bulk thermoelectrics via a panoscopic approach. *Mater Today* 16:166–176
- [3] Lwin ML, Dharmiah P, Min BH et al (2021) Tuning of thermoelectric transport properties via the formation of hierarchical structures in Bi-doped $\text{Gd}_2\text{O}_3/\text{Bi}_{0.5}\text{Sb}_{1.5}\text{Te}_3$ nanocomposites. *Int J Energy Res* 45:20921–20933
- [4] Ma Z, Wei J, Song P et al (2021) Review of experimental approaches for improving zT of thermoelectric materials. *Mater Sci Semicond Process* 121:105303
- [5] Zhu H, Xiao C, Xie Y (2018) Design of highly efficient thermoelectric materials: tailoring reciprocal-space properties by real-space modification. *Adv Mater* 30:1802000
- [6] Liu W, Hu J, Zhang S et al (2017) New trends strategies and opportunities in thermoelectric materials: a perspective. *Mater Today Phys* 1:50–60
- [7] Chang C, Zhao L-D (2018) Anharmonicity and low thermal conductivity in thermoelectrics. *Mater Today Phys* 4:50–57
- [8] Luo Y, Cai S, Hua X et al (2019) High thermoelectric performance in polycrystalline SnSe via dual-doping with Ag/Na and nanostructuring with Ag_8SnSe_6 . *Adv Energy Mater* 9:1803072
- [9] Zhang Q, Song Q, Wang X et al (2018) Deep defect level engineering: a strategy of optimizing the carrier concentration for high thermoelectric performance. *Energy Environ Sci* 11:933–940
- [10] Chandra S, Biswas K (2019) Realization of high thermoelectric figure of merit in solution synthesized 2D SnSe nanoplates via Ge alloying. *J Am Chem Soc* 141:6141–6145
- [11] Li X, Liu J, Li S et al (2020) Synergistic band convergence and endotaxial nanostructuring: achieving ultralow lattice thermal conductivity and high figure of merit in eco-friendly SnTe. *Nano Energy* 67:104261
- [12] Deng H, Lou X, Lu W et al (2021) High-performance eco-friendly MnTe thermoelectrics through introducing SnTe nanocrystals and manipulating band structure. *Nano Energy* 81:105649
- [13] Tan G, Shi F, Hao S et al (2015) Codoping in SnTe: enhancement of thermoelectric performance through synergy of resonance levels and band convergence. *J Am Chem Soc* 137:5100–5112
- [14] Zhang Q, Ti Z, Zhu Y et al (2021) Achieving ultralow lattice thermal conductivity and high thermoelectric performance in

- GeTe alloys via introducing Cu₂Te nanocrystals and resonant level doping. *ACS Nano* 15:19345–19356
- [15] Li S, Lou X, Zou B et al (2021) Introducing PbSe quantum dots and manipulating lattice strain contributing to high thermoelectric performance in polycrystalline SnSe. *Mater Today Phys* 21:100542
- [16] Kim SI, Lee KH, Mun HA et al (2015) Dense dislocation arrays embedded in grain boundaries for high-performance bulk thermoelectrics. *Science* 348:109–114
- [17] Lou X, Li S, Chen X et al (2021) Lattice strain leads to high thermoelectric performance in polycrystalline SnSe. *ACS Nano* 15:8204–8215
- [18] Biswas K, He J, Blum ID et al (2012) High-performance bulk thermoelectrics with all-scale hierarchical architectures. *Nature* 489:414–418
- [19] Wang FQ, Zhang S, Yu J, Wang Q (2015) Thermoelectric properties of single-layered SnSe sheet. *Nanoscale* 7:15962–15970
- [20] Biswas K, He J, Zhang Q et al (2011) Strained endotaxial nanostructures with high thermoelectric figure of merit. *Nat Chem* 3:160–166
- [21] Liu Z, Mao J, Liu T-H et al (2018) Nano-microstructural control of phonon engineering for thermoelectric energy harvesting. *MRS Bull* 43:181–186
- [22] Zhao Q, Qin B, Wang D et al (2019) Realizing high thermoelectric performance in polycrystalline SnSe via silver doping and germanium alloying. *ACS Appl Energy Mater* 3:2049–2054
- [23] Xiao Y, Zhao L-D (2020) Seeking new, highly effective thermoelectrics. *Science* 367:1196–1197
- [24] Shi W, Gao M, Wei J et al (2018) Tin selenide (SnSe): growth, properties, and applications. *Adv Sci* 5:1700602
- [25] Albrecht S, Reining L, Del Sole R, Onida G (1998) Ab initio calculation of excitonic effects in the optical spectra of semiconductors. *Phys Rev Lett* 80:4510
- [26] Peng K, Zhang B, Wu H et al (2018) Ultra-high average figure of merit in synergistic band engineered Sn_xNa_{1-x}Se_{0.9}S_{0.1} single crystals. *Mater Today* 21:501–507
- [27] Kutorasinski K, Wiendlocha B, Kaprzyk S, Tobola J (2015) Electronic structure and thermoelectric properties of n- and p-type SnSe from first-principles calculations. *Phys Rev B* 91:205201
- [28] Kang JS, Wu H, Li M, Hu Y (2019) Intrinsic low thermal conductivity and phonon renormalization due to strong anharmonicity of single-crystal tin selenide. *Nano Lett* 19:4941–4948
- [29] Zhao L-D, Lo S-H, Zhang Y et al (2014) Ultralow thermal conductivity and high thermoelectric figure of merit in SnSe crystals. *Nature* 508:373–377
- [30] Zhao L-D, Chang C, Tan G, Kanatzidis MG (2016) SnSe: a remarkable new thermoelectric material. *Energy Environ Sci* 9:3044–3060
- [31] Chattopadhyay T, Pannetier J, Von Schnering HG (1986) Neutron diffraction study of the structural phase transition in SnS and SnSe. *J Phys Chem Solids* 47:879–885
- [32] Duvjir G, Min T, Thi Ly T et al (2017) Origin of p-type characteristics in a SnSe single crystal. *Appl Phys Lett* 110:262106
- [33] Leng H-Q, Zhou M, Zhao J et al (2016) The thermoelectric performance of anisotropic SnSe doped with Na. *RSC Adv* 6:9112–9116
- [34] Guo R, Wang X, Kuang Y, Huang B (2015) First-principles study of anisotropic thermoelectric transport properties of IV-VI semiconductor compounds SnSe and SnS. *Phys Rev B* 92:115202
- [35] Peng K, Lu X, Zhan H et al (2016) Broad temperature plateau for high ZT s in heavily doped p-type SnSe single crystals. *Energy Environ Sci* 9:454–460
- [36] Zhao L-D, Tan G, Hao S et al (2016) Ultrahigh power factor and thermoelectric performance in hole-doped single-crystal SnSe. *Science* 351:141–144
- [37] Qin B, Wang D, He W et al (2018) Realizing high thermoelectric performance in p-type SnSe through crystal structure modification. *J Am Chem Soc* 141:1141–1149
- [38] Qin B, Zhang Y, Wang D et al (2020) Ultrahigh average ZT realized in p-type SnSe crystalline thermoelectrics through producing extrinsic vacancies. *J Am Chem Soc* 142:5901–5909
- [39] Jin M, Shi X-L, Feng T et al (2019) Super large Sn_{1-x}Se single crystals with excellent thermoelectric performance. *ACS Appl Mater Interfaces* 11:8051–8059
- [40] Wei W, Chang C, Yang T et al (2018) Achieving high thermoelectric figure of merit in polycrystalline SnSe via introducing Sn vacancies. *J Am Chem Soc* 140:499–505
- [41] Pauling L (1932) The nature of the chemical bond. IV. The energy of single bonds and the relative electronegativity of atoms. *J Am Chem Soc* 54:3570–3582
- [42] Sun J, Yu J, Guo Y, Wang Q (2020) Enhancing power factor of SnSe sheet with grain boundary by doping germanium or silicon. *npj Comput Mater* 6:1–6
- [43] Wei T-R, Tan G, Zhang X et al (2016) Distinct impact of alkali-ion doping on electrical transport properties of thermoelectric p-type polycrystalline SnSe. *J Am Chem Soc* 138:8875–8882
- [44] Chen C-L, Wang H, Chen Y-Y et al (2014) Thermoelectric properties of p-type polycrystalline SnSe doped with Ag. *J Mater Chem A* 2:11171–11176

- [45] Blöchl PE, Jepsen O, Andersen OK (1994) Improved tetrahedron method for Brillouin-zone integrations. *Phys Rev B* 49:16223
- [46] Kresse G, Hafner J (1993) Ab initio molecular dynamics for liquid metals. *Phys Rev B* 47:558
- [47] Kresse G, Hafner J (1994) Ab initio molecular-dynamics simulation of the liquid-metal–amorphous-semiconductor transition in germanium. *Phys Rev B* 49:14251
- [48] Perdew JP, Burke K, Ernzerhof M (1996) Generalized gradient approximation made simple. *Phys Rev Lett* 77:3865
- [49] Tran F, Blaha P (2009) Accurate band gaps of semiconductors and insulators with a semilocal exchange-correlation potential. *Phys Rev Lett* 102:226401
- [50] Krukau AV, Vydrov OA, Izmaylov AF, Scuseria GE (2006) Influence of the exchange screening parameter on the performance of screened hybrid functionals. *J Chem Phys* 125:224106
- [51] Madsen GKH, Carrete J, Verstraete MJ (2018) BoltzTraP2, a program for interpolating band structures and calculating semi-classical transport coefficients. *Comput Phys Commun* 231:140–145
- [52] Hedin L (1965) New method for calculating the one-particle Green's function with application to the electron-gas problem. *Phys Rev* 139:A796
- [53] Rohlfing M, Louie SG (1998) Electron-hole excitations in semiconductors and insulators. *Phys Rev Lett* 81:2312
- [54] Karunaratne A, Gladden JR, Priyadarshan G et al (2018) Room temperature resonant ultrasound spectroscopy of single crystalline SnSe. *ACS Appl Energy Mater* 1:6123–6128
- [55] Sattar MA, Benkraouda M, Amrane N (2022) First-principles study on the structural, electronic, vibrational, and optical properties of the Ru-doped SnSe. *Phys B* 633:413789
- [56] Kim HS, Choi G, Ha MY et al (2019) Thermoelectric transport properties of Pb doped SnSe alloys ($\text{Pb}_x\text{Sn}_{1-x}\text{Se}$): DFT-BTE simulations. *J Solid State Chem* 270:413–418
- [57] Csonka GI, Perdew JP, Ruzsinszky A et al (2009) Assessing the performance of recent density functionals for bulk solids. *Phys Rev B* 79:155107
- [58] Carrete J, Mingo N, Curtarolo S (2014) Low thermal conductivity and triaxial phononic anisotropy of SnSe. *Appl Phys Lett* 105:101907
- [59] González-Romero RL, Antonelli A, Meléndez JJ (2017) Insights into the thermoelectric properties of SnSe from ab initio calculations. *Phys Chem Chem Phys* 19:12804–12815
- [60] Sham LJ, Schlüter M (1985) Density-functional theory of the band gap. *Phys Rev B* 32:3883
- [61] Yang J, Zhang G, Yang G et al (2015) Outstanding thermoelectric performances for both p-and n-type SnSe from first-principles study. *J Alloy Compd* 644:615–620
- [62] Ma J, Chen Y, Li W (2018) Intrinsic phonon-limited charge carrier mobilities in thermoelectric SnSe. *Phys Rev B* 97:205207
- [63] Lee YK, Ahn K, Cha J et al (2017) Enhancing p-type thermoelectric performances of polycrystalline SnSe via tuning phase transition temperature. *J Am Chem Soc* 139:10887–10896
- [64] Escudero D, Duchemin I, Blase X, Jacquemin D (2017) Modeling the photochrome– TiO_2 interface with Bethe-Salpeter and time-dependent density functional theory methods. *J Phys Chem Lett* 8:936–940
- [65] Körbel S, Kammerlander D, Sarmiento-Pérez R et al (2015) Optical properties of Cu-chalcogenide photovoltaic absorbers from self-consistent G W and the Bethe-Salpeter equation. *Phys Rev B* 91:075134
- [66] Born M, Huang K, Lax M (1955) Dynamical theory of crystal lattices. *Am J Phys* 23:474–474
- [67] Li G, Aydemir U, Wood M et al (2017) Ideal strength and deformation mechanism in high-efficiency thermoelectric SnSe. *Chem Mater* 29:2382–2389
- [68] Wu Z, Zhao E, Xiang H et al (2007) Crystal structures and elastic properties of superhard Ir N_2 and Ir N_3 from first principles. *Phys Rev B* 76:054115
- [69] Hill R (1952) The elastic behaviour of a crystalline aggregate. *Proc Phys Soc Sect A* 65:349
- [70] Xiao Y, Chang C, Pei Y et al (2016) Origin of low thermal conductivity in SnSe. *Phys Rev B* 94:125203
- [71] Sattar MA, Javed M, Benkraouda M, Amrane N (2021) The structural stability, lattice dynamics, electronic, thermophysical, and mechanical properties of the inverse perovskites A_3OX : a comparative first-principles study. *Int J Energy Res* 45:4793–4810
- [72] Shi X, Zheng K, Hong M et al (2018) Boosting the thermoelectric performance of p-type heavily Cu-doped polycrystalline SnSe via inducing intensive crystal imperfections and defect phonon scattering. *Chem Sci* 9:7376–7389

Publisher's Note Springer Nature remains neutral with regard to jurisdictional claims in published maps and institutional affiliations.

Springer Nature or its licensor (e.g. a society or other partner) holds exclusive rights to this article under a publishing agreement with the author(s) or other rightsholder(s); author self-archiving of the accepted manuscript version of this article is solely governed by the terms of such publishing agreement and applicable law.